Biosensors and Bioelectronics 109 (2018) 184–189

Contents lists available at ScienceDirect

Biosensors and Bioelectronics

journal homepage: www.elsevier.com/locate/bios

Signal amplification strategy for biomarkers: Structural origins of epitaxial-growth twinned nanocrystals and D–π–A type polymers

He Liu[a], Yue Gu[a], Tao Dong[b], Liuqing Yan[a], Xiaoyi Yan[a], Tingting Zhang[a], Nannan Lu[a], Zhiqian Xu[a], Haixin Xu[a], Zhiquan Zhang[a,*], Ting Bian[c,*]

[a] College of Chemistry, Jilin University, Changchun 130012, PR China
[b] Department of Chemistry, University of Washington, Seattle, WA 98195-1700, United States
[c] School of Energy and Power Engineering, Jiangsu University of Science and Technology, Zhenjiang 212003, PR China

ARTICLE INFO

Keywords:
Epitaxial-growth twinned nanocrystals
Linear donor–π–acceptor polymers
Charge-transfer
Electrochemical immunosensors
H_2O_2 reduction reaction

ABSTRACT

The combination of nanoparticles and biomarkers yields functional nanostructured biointerface, which is playing a notable role in biotechnology development. Due to the 5-fold twined structure in the Au-Pt star-shaped decahedra not only allowed it to act as efficient scaffold for immobilization of antibody, but it also exhibits superior electrocatalytic activity toward H_2O_2 reduction, the nanocrystal as the efficient signal transduction label is first employed to construct an electrochemical immunosensor. Donor–π–Acceptor (D–π–A) linking fashion generates a dipolar push-pull system and assures superior intramolecular charge transfer. It is considered as a suitable π-conjugated backbone for conducting polymer on biointerface application. Under a D–π–A architecture which imidazole as the π-bridge and amino phenyl/phenyl groups as peripheral electron-donating/withdrawing functional groups, 4-(2,4,5-triphenyl-1H-imidazol-1-yl) aniline (TPIDA) is designed and synthesized for good biocompatibility and high conductivity. In this proposal, we attempt to integrate the above-mentioned two features from nanobiotechnology and organic bioelectronics. Then, a novel nonenzymatic sandwich-type immunosensor is performed by Au-Pt core-shell with surface-engineered twinning as a label and π-conjugated D–π–A polymers as the signal amplification platform. Human IgG (HIgG) as the model target protein can be detected with a wide linear range from 0.1 pg mL^{-1} to 100 ng mL^{-1}. The detection limit is down to 0.06 pg mL^{-1} (S/N = 3). Moreover, as a practical application, the prepared biosensor is used to monitor HIgG level in human serum with desirable results obtained.

1. Introduction

Biomarker, as an indicator of biological state or pharmacological response, has been used for objectively measuring and evaluation in early clinical diagnosis and prognosis (Golubnitschaja and Flammer, 2007). A credible detection of low-abundance (in the pg mL^{-1} range) protein biomarkers continues to be a serious issue (Tang et al., 2016). And clinical practices are no longer implemented merely in the laboratory setup (Travers, 2002). Compared with other immunoassay methodologies including fluorescence (Ranzoni et al., 2015), surface-enhanced electrochemiluminescence (Wang et al., 2015a), enzyme-linked immunosorbent assay (Ran et al., 2017) and chemiluminescence (Zhag et al., 2014), electrochemical immunosensor stands out because of its operational simplicity, feasible miniaturization, and subsequent portability (Kang et al., 2017; Lin et al., 2015; Qi et al., 2016). Up to now, several elegant electrochemical strategies have been developed, such as amperometry, potentiometry, voltammetry and impedance (Wen et al., 2017). Among these transducer methods, the sandwich-type amperometric protocol provides ultrasensitive and specific detection in both reported researches and commercial assays due to the use of two matched antibodies.

For sandwich-type electrochemical immunosensors, their excellent sensitivity are tightly related to generated current responses (ΔI) which are caused by the labeled antibodies binding with the analytes and significantly influenced by the conductivity of the sensing interfaces. However, because of the poor conductivity of proteins, the high-impedance layers are easily formed between antigens-antibodies and blocking reagents, which greatly affect the sensitivity and reliability of the biosensor (Gao et al., 2013; Wu and Qu, 2015). Hence, further progress is picking by using various signal transduction labels to probe immunoreactions. Some researches have looked to develop enzyme like activity of metallic nanoparticles, controlling and tailoring their unique properties to offer novel approaches for carrying higher contents of signal tags. In this respect, Pt nanocatalysts as the promising candidates

* Corresponding authors.
E-mail addresses: zzq@jlu.edu.cn (Z. Zhang), biantingbest@163.com (T. Bian).

https://doi.org/10.1016/j.bios.2018.03.016
Received 9 January 2018; Received in revised form 7 March 2018; Accepted 8 March 2018
Available online 13 March 2018
0956-5663/

extend the functions of nanocarriers and nanozymes, displaying excellent catalytic ability, conductivity, biocompatibility and long-term stability (Kulhanek and Bures, 2012; Pedone et al., 2017; Song et al., 2014; Wang et al., 2016). Au-Pt nanocrystals are more attractive for facilitating the redox reactions compared with their single-crystal counterparts, owing to the changes in the atomic spatial arrangement and electronic structure (Bian et al., 2015; Gao et al., 2015; Gilroy et al., 2016; Yamauchi et al., 2012). The catalytic performance of bimetallic nanohybrid is extraordinarily sensitive to the structural parameters including size, facet, interface, internal structure and surface shape. Some mechanisms for reactivity of twin boundary defects resulting from their inherently strained structure offer further explanations of the superior catalytic activity of nanocrystals (Walsh et al., 2017; Wang et al., 2015b; Wu et al., 2012). Au-Pt core-shell star-shaped decahedra catalysts for oxygen reduction reaction exhibited the distinct extent of enhanced activity and durability, which can be associated with their active sites at the twin boundaries and strain-induced electronic effects (Bian et al., 2015). Hence we infer that the combination of such intriguing nanomaterials and biomolecules can yield functional nanostructured biointerfaces with the surprising characteristic of catalytic decomposition of H_2O_2, they provide an effective solution for a nonenzymatic electrochemical immunosensor.

Besides investigating the electrocatalytic performance of Au-Pt star-shaped decahedra as a label, the immobilization of primary antibody (Ab_1) on the modified electrode with superior charge transfer is another pivotal step for the increase of sensitivity of the immunosensor. Conducting polymers have received great attention due to their excellent electrical properties, which bridge the gap between electronics and biochemistry (Hackett et al., 2017; Liu et al., 2018; Simon et al., 2016). Additionally, the fabrication of conducting polymers take the advantage of the flexible monomer design by introducing amino or carboxyl groups to covalently attach antibodies (Aydemir et al., 2016). This strategy provides a direct electrical readout to avoid extra conjugation reactions which passivate the electrode from performing faradaic electrochemistry (Gao et al., 2015). Designing π-conjugated compounds with donor–π–acceptor (D–π–A) structures in most recently literature are finding applications in organic light-emitting diode (Sun et al., 2014), photovoltaiccells (Long et al., 2017; Melkonyan et al., 2016), organic field-effect transistors (Ashraf et al., 2015) and circuitry (Tobjörk and Österbacka, 2011) due to their tunable optical and electrical properties (Kulhanek and Bures, 2012). Their catalytic properties as signal amplifiers in electrochemical biosensors are seldom presented. Based on those facts, we reason that introducing aminophenyl on D–π–A conjugated polymers can create a novel biosensing platform capable of monitoring biospecific interactions by accelerating the electron transfer rate between the analytes and the electrode system.

Inspired by exploring the structure-property relationship that is performed by systematically altering the π-linker, imidazole-derived push-pull system has drawn our attention because it possesses two nitrogen atoms of distinctive electronic nature (Kulhánek and Bureš, 2012; Molina et al., 2012). There is considerable interest among scientists for their remarkable biological and pharmacological activities, such as anticancer, antibacterial, antifungal, etc (Ali et al., 2017). In particular, the structural of the imidazole heterocycle with electron rich characteristic is favorable for imidazole-based molecule to readily bind with diverse enzymes and protein molecules (Sharma et al., 2014). Since the functionalized imidazole derivatives play crucial roles in the realms of chemistry and biomedicine, we believe that these may emerge as the transducers of the biological recognition events for electrochemical immunosensors. In order to focus on the high conjugation degree aromatic nature, employing imidazole as the π-bridge to connect with the electron-donating/withdrawing aminophenyl/phenyl groups for constructing the D–π–A architecture has been taken into consideration. As a result of concept, 4-(2,4,5-triphenyl-1H-imidazol-1-yl) aniline (TPIDA) has been designed with excellent conductivity and innate “biocompatibility”. The π-orbitals of TPIDA are delocalized along the molecule and their conjugated oligomers are gained through a facile electrochemical method.

Base on the intense interest stems from both biocompatible nanomaterials with enzymatic properties and conducting polymers for electrochemical sensing, a unique nonenzymatic sandwich-type immunosensor is performed by Au-Pt core-shell with surface-engineered twinning as a label and π-conjugated D–π–A polymer as a the signal amplification platform. Compared with the previously reported approaches, two main elements are introduced to exquisitely improve the analytical performance for immunoassay, namely: (1) The 5-fold twined structure in the Au-Pt star-shaped decahedra not only allowed it to act as efficient scaffold for immobilization of antibody, but it also exhibits superior electrocatalytic activity toward H_2O_2 reduction, which should be attributed to its highly active sites at the twin boundaries with support-induced strain. (2) A high degree of D–π–A conjugated polymer is first obtained via ingenious transition of the structure and length of oligomer from the spherical monomers to microwire-like polymer, invoking extended electronic communication and transport for signal amplification.

2. Experimental

2.1. Reagents and apparatus

The reagents used for the synthesis and detection and the apparatus parameters are listed in the Supporting information.

2.2. Synthesis of the TPIDA monomer

TPIDA monomer was synthesized according to the previous report with a slight modification (Yan et al., 2017). Briefly, aryl diketone was prepared according to the published procedure (Saikachi and Matsuo, 1964). The mixtures of p-phenylenediamine (0.5 mmol), aryl diketone (1 mmol), silica gel (0.5 g), benzaldehyde (1 mmol), ammonium acetate (4 mmol) and $H_3[PW_{12}O_{40}]$ (0.7%) were completely ground in a mortar and transferred to a flask (25 mL). It was then heated with microwave irradiation for 15 min at 130 °C and cooled to room temperature. The reaction procedure was monitored by TLC on Silufol-254 plates. The crude product was purified by chromatography on silica gel (petroleum ether/ethyl acetate = 3/1 as eluent) and then recrystallized in ethanol to give the product (yield 78%).

2.3. Synthesis of Au-Pt core-shell star-shaped decahedra

The synthesis route was based on our previous work (Bian et al., 2015). Briefly, 150 mg of hexadecyltrimethyl ammonium bromide (CTAB), 50 mg of trioctylphosphine oxide (TOPO) and 3 mL of oleylamine were dissolved and stirred at 180 °C in air. Meanwhile, 6.2 mg of $HAuCl_4$ and 7.75 mg of H_2PtCl_6 were added into 1.5 mL of oleylamine to give the precursor as a yellow solution. Subsequently, the precursor solution was rapidly poured into the hot solution containing TOPO and CTAB with a pipette. The obtained solution maintained heating at 180 °C for 3 h in air. Finally, the suspension was centrifuged and washed three times with ethanol and hexane to remove solvent of oleylamine, CTAB, and TOPO.

2.4. Phase transfer of Au-Pt nanocrystal from the organic to the aqueous phase

As synthesized, these well-defined nanocrystals are typically generated from organic solution synthesis. Therefore, the surface decoration step is even more important to develop a multifunctional ligand system that makes them hydrophilic and stable against agglomeration and also provides high biostability in a biological system (Jun et al., 2005; Xie et al., 2007). With the modified procedure (Jun et al., 2005), Au-Pt core-shell nanocrystals (10 mg) with desired shapes were

dissolved in 1 mL of toluene and 2,3-dimercaptosuccinic acid molecules (10 mg) were added in 1 mL of dimethyl sulfoxide (DMSO). Then the two kinds of solution were mixed and the precipitate of black powders were isolated by centrifugation.

2.5. Preparation of Au-Pt nanocrystal-Ab_2 as label

The synthesized Au-Pt nanocrystal (0.1 mg) and mouse anti-human IgG (Ab_2) (5 μL, 0.1 mg mL^{-1}) were dispersed into 1 mL of phosphate buffer solution (PBS, pH = 7.4) under stirring. Then, the mixture was incubated at 4 °C for 12 h and washed with PBS (pH 7.4) to remove unbounded Ab_2 in consecutive centrifugation. Afterwards, the final product (Au-Pt nanocrystal-Ab_2) was dissolved in PBS and stored at 4 °C before using.

2.6. Sandwich-type electrochemical immunosensing

Prior to modification, the glassy carbon electrode (GCE) was polished by 1.0, 0.3 and 0.05 μm alumina powders respectively and sonicated in 1:1 nitric acid, ethanol and water, each for 1 min. The fabrication process of the immunosensor was prepared by step-wise, as outlined in Scheme 1. Initially, the electropolymerization of TPIDA on pretreated GCE surface was performed in N,N-dimethylformamide/acetonitrile = 3:2 (v/v) solution consisting of 1.000 mg mL^{-1} TPIDA monomer, in the presence of 100.0 mM $LiClO_4$ as a supporting electrolyte by cyclic sweeping from − 1.0 to 1.4 V (versus Ag wire) at 0.10 V s^{-1} for 40 cycles. After polymerization, the GCE was cleaned with large volumes of acetonitrile to remove the supporting electrolyte and monomers. Then, 5 μL of 100 μg mL^{-1} rabbit anti-human IgG (Ab_1) were dropped on the polymer modified GCE, which was incubated at 4 °C overnight to provide cross linkages between the Ab_1 and amino groups of the polymer. After reaction, the resultant GCE was washed with PBS and incubated in 1 wt% BSA solution for 1 h to eliminate the nonspecific binding effect. After another washing with PBS, 5 μL of human IgG (HIgG) solution at a specific concentration was coated onto the GCE and dried at room temperature, followed by washing with PBS. Thereafter, 5 μL of 1 mg mL^{-1} Au-Pt nanocrystal-Ab_2 was further dropped onto the GCE and left to dry naturally at room temperature. After rinsing, the immunosensor was obtained and placed in an electrochemical cell for measurements.

3. Results and discussions

3.1. Characterizations of the Au-Pt nanocrystal and its binding Ab_2

Precisely controlled crystal synthesis offers enabling platforms for understanding of catalysis and sensing. A TEM study on decahedral Au-Pt nanoparticles displays good monodispersity and star-like shape with an average size of 16 nm (Fig. 1a). The HRTEM image clearly shows that an individual star-shaped decahedron is made up of five single-crystalline domains bound by twin-based adjoining planes (Fig. 1b). It is well-established that the nanocrystals with twinned structures can exhibit highly desirable catalytic properties due to the surface strain (Wang et al., 2015b). In addition, as shown in Fig. 1b, the lattice constant is calculated to be 2.30 Å, indicating that the exposed facets are dominated by (111) planes. It has been demonstrated that the specific activity of Pt (111) towards oxygen reduction reaction is at least twice that of Pt (100) (Wang et al., 2015b; Wu et al., 2012). Therefore, the twinned Au-Pt decahedra can be considered as not only nanocarrier to anchor large amounts of Ab_2 but rather a nanocatalyst to catalyze H_2O_2 in virtue of its (111) facets and twin defects on its surfaces. Star-shaped decahedrons are also validated by HAADF-STEM in Fig. 1c. The elemental distribution of Au-Pt core-shell structure is determined by EDS line-scan analysis (Fig. 1d). As observed, the Au has one intensity peak in the center, whereas the Pt has two intensity peaks at two ends, revealing the core-shell structure in a single nanoparticle. To offer preliminary insight into the nanoparticles/antibody nanobiointerface and their surface binding ability, TEM images have been obtained to assess how decahedral Au-Pt nanoparticles prefer to reside upon Ab_2 surfaces. It is evident from Fig. 1e that when the Ab_2 are tagged with Au-Pt nanoparticles, the compound are well dispersed in PBS and stable without aggregation. This is attributed to the high quality biocompatible Au-Pt nanoparticles which is attained through environmentally friendly preparation. Fig. 1f is further supporting the conclusion that the star shape nature of the nanoparticles has interacted with Ab_2. And the electrochemical signal of the unique nanostructure tagged Ab_2 to the detection of H_2O_2 is investigated. Fig. 3 a shows the cyclic voltammogram (CV) measurement of Au-Pt nanocrystal-Ab_2 modified electrode in N_2-saturated PBS in the absence and presence of H_2O_2. A dramatic increase of the cathodic current was observed for the Au-Pt nanocrystal-Ab_2 with adding 5 mM H_2O_2, which is higher than that previous reported (Qin et al., 2011). The result demonstrates that the functional nanostructured biointerfaces indeed endowed high catalytic activity in the process of H_2O_2 electrocatalytical reduction.

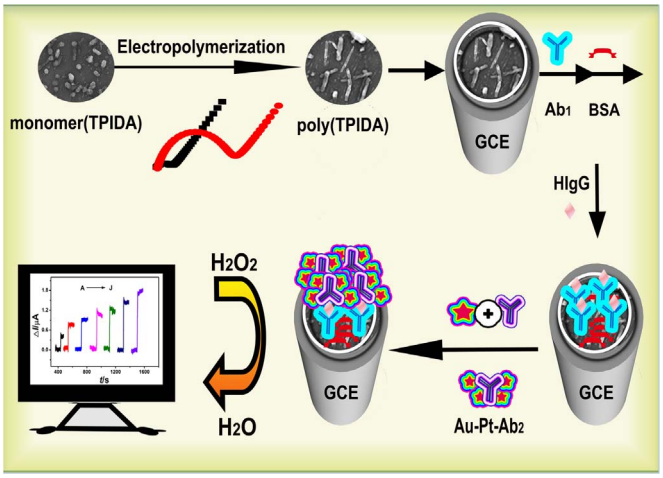

Scheme 1. Work flow diagram for biosensor development.

3.2. Electropolymerization of TPIDA

Fig. S1 displays the growth process of the TPIDA film on GCE surface via successive CVs. At about 1.0 V the oxidation of tertiary amino and formation of a radical cation occur (Ashok et al., 2009). The couple of redox peaks at more negative potential (centred at around – 0.6 V) corresponds to redox process of the monomers. As can be seen, the peak currents increase gradually during the repeated potential scans, indicative of the formation of conductive polymer film at the GCE surface. There are few reports concerning the mechanism for the electropolymerization of imidazole. A hypothesis for structure of nile blue, which pointed out the possibility of carbon-nitrogen coupling upon radical dimerization, was taken into account (Chen et al., 2008; Kul et al., 2011). Herein, the unpaired electron in the radical cation may attack either the amine group or the neighboring ortho carbon atom to form a mixture of dimeric and trimeric species. The possible electropolymerization path of TPIDA is shown in Fig. S2.

3.3. Characterizations of TPIDA monomer, poly(TPIDA) and poly(TPIDA)-Ab_1

Figs. S3 and S4 offer a ^1H NMR spectrum and a FT-IR spectra of TPIDA in Supplementary information. The electrochemical performances of poly(TPIDA) were optimized regarding the polymerized conditions, such as the potential range (especially the upper limit), the scan rate and scan cycles applied to the electrode during the formation of the polymer film. Since all electropolymerization parameters

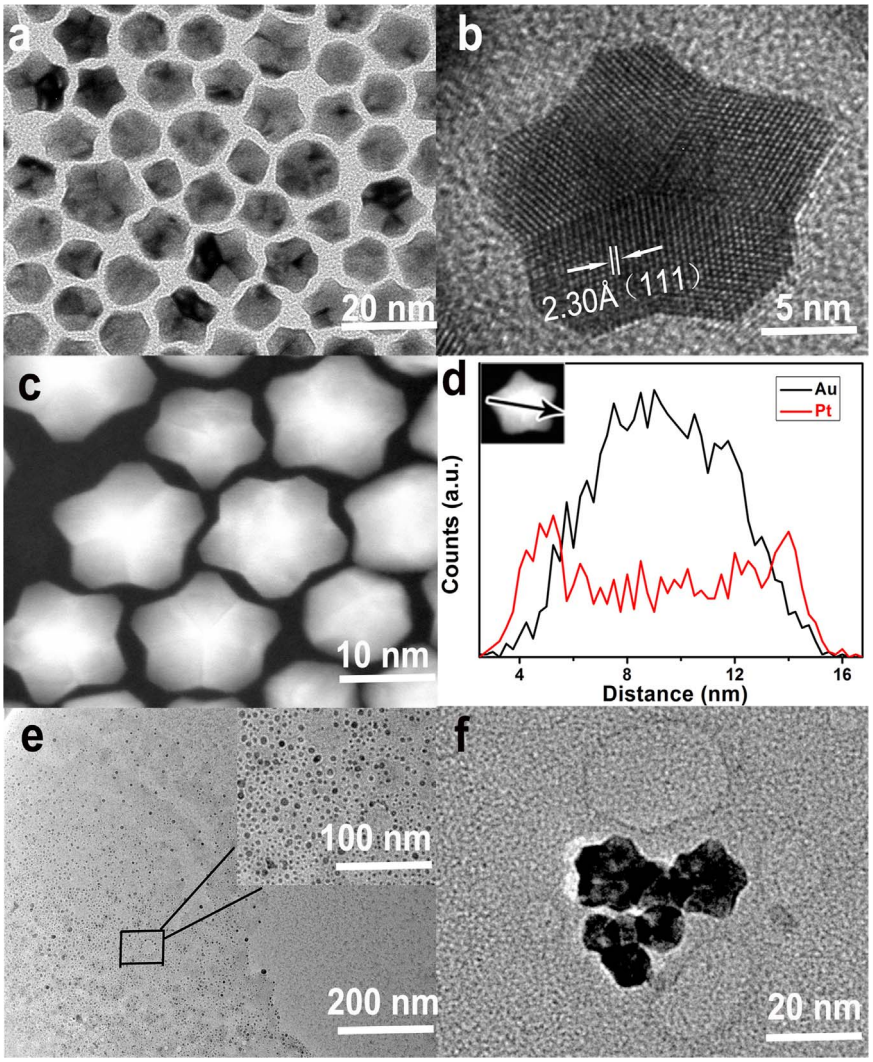

Fig. 1. (a) TEM image, (b) HRTEM image, (c) HAADF-STEM image, (d) EDX line-scan analysis of Au-Pt star-shaped decahedra. (e) TEM image of Au-Pt-Ab_2. Inset: TEM image at a higher magnification. (f) Magnified TEM image of a couple of star-shaped decahedron and Ab_2.

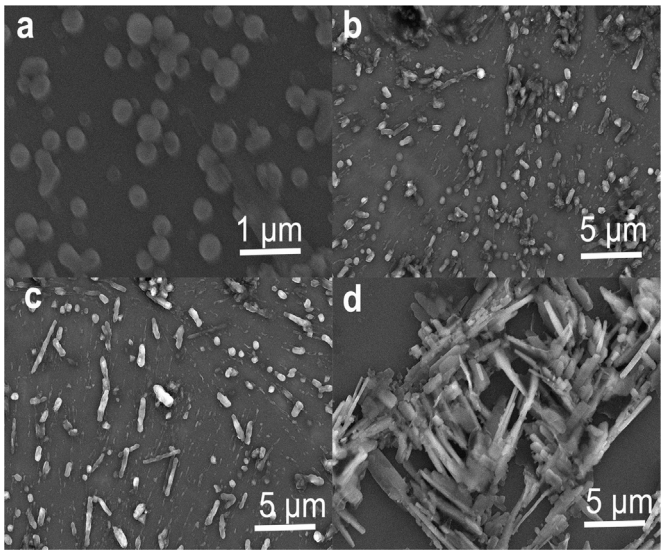

Fig. 2. SEM image of (a) TPIDA monomers, (b) poly(TPIDA) by CV scanning for 20 cycles and (c) poly(TPIDA) by CV scanning for 40 cycles in the dimethyl sulfoxide/acetonitrile = 3:2 (v/v) solution in the presence of 1.00 mg mL^{-1} TPIDA and 100.0 mM LiClO4 as supporting electrolyte, (d) poly(TPIDA)-Ab_1.

examined here were optimal, we found an interesting phenomenon about the influence of the number of potential cycles on the materials morphological changes. As shown in Fig. 2a, the morphology of TPIDA monomers are spherical and the sizes are in the range of 0.3–0.5 μm. Nevertheless, by varying the scan cycles in the range from 20 (Fig. 2b) to 40 (Fig. 2c), the globules are orderly connected into stick-like microwires ranging from 0.5 to 5 μm. After 40 scans, the equilibrium of microwires are attained with an maximum average size of 5 μm. We postulate that the backbones interaction of the large-scale π-conjugation induced the oligomer molecules to linear growth during the reaction. Fig. 2d, where the formation of immunocomplex between the poly (TPIDA) and Ab_1 which was lead poly(TPIDA) covered with white material, confirming that electropolymerization is an effective method for forming three-dimensional coating and providing larger accessible surface with an innate biocompatibility. There are few reports on D–π–A based polymers, and even less on the explanation of their morphologies and electronic structures in relevant electrophysiological sensing field, although controlling electron transfer theory through short molecular wires has been used in the realms of magnetic field andoptical transduction (Gu et al., 2015; Swager, 1998). This conjugation between each repeated unit gives birth of semiconductive "molecular wires", providing the polymer with superior electronic properties due to its robust conductivity of the backbone. The electrochemical impedance spectroscopy (EIS) and CV were recorded to

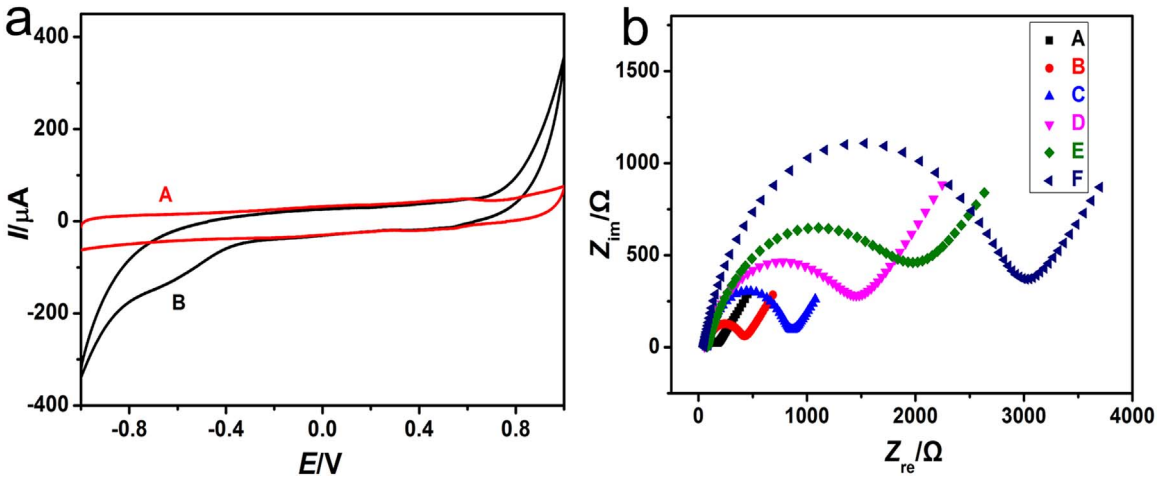

Fig. 3. (a) CVs of the Au-Pt nanocrystal-Ab_2 modified electrode in N_2-saturated 0.1 M PBS (pH = 7.4) without (curve A) and with (curve B) 5 mM H_2O_2. Scan rate: 0.10 V s^{-1}. (b) The EIS of poly(TPIDA)/GCE (curve A), bare GCE (curve B), poly(TPIDA)/Ab_1/GCE (curve C), poly(TPIDA)/Ab_1/BSA/GCE (curve D), poly(TPIDA)/Ab_1/BSA/HIgG/GCE (curve E), poly(TPIDA)/Ab_1/BSA/HIgG/Au-Pt-Ab_2/GCE (curve F) were conducted from 0.1 to 100 kHz in 0.1 M KCl solution including 10 mM $Fe(CN)_6^{3-}$/$Fe(CN)_6^{4-}$.

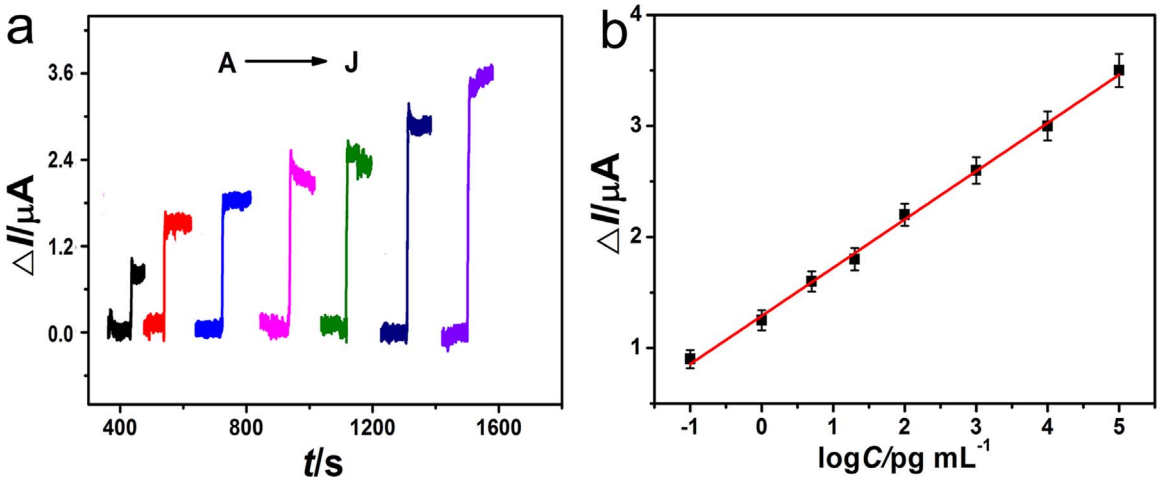

Fig. 4. (a) Amperometric response (ΔI) of the immunosensor, wherein different concentrations of HIgG (A – J: 0.1 pg mL^{-1} to 100 ng mL^{-1}) used for detection. (b) Plot of modulus ΔI against logarithmic value of HIgG concentration used.

validate the explanation for the polymerization process. Fig. S5a shows the Nyquist plots at the bare GCE, monomer coated GCE and the poly (TPIDA)/GCE modified with different scan circles. The EIS data were fitted to an equivalent circuit (inset of Fig. S5a), and the charge transfer resistance (R_{ct}) values of the modified electrodes were obtained by calculating the diameter of semicircles in the plot (Guo et al., 2012). It was found that the Rct of the bare GCE (curve C) and monomer coated GCE (curve D) were 321.3 Ω and 422.9 Ω. In contrast, the R_{ct} value for poly(TPIDA) film with 20 CVs was decreased to 208.5 Ω (curve B). On the 40th CVs poly(TPIDA) film (curve A), the smallest R_{ct} was 91.3 Ω. When the length of the linear polymermolecules increases, its charge transfer rate increases, suggesting that the molecular wires as key feature of the conducting polymer provide an extended electronic communication and higher mobility. Next, CVs were considered to provide electrochemical evidence for the electrode materials of TPIDA and poly (TPIDA). As indicated in Fig. S5b, the poly(TPIDA)/GCE gives a larger current response in comparison with the bare GCE and monomer coated GCE, which agrees with the impedance sensing change Fig. 4.

3.4. Characterization of the assembly procedure of immunosensor

The immunosensor configuration after each fabricated step was confirmed by EIS measurements (Fig. 3b). It was obvious to see that R_{ct} for the bare GCE(321.3 Ω) (curve B) is larger than the GCE modified with poly(TPIDA) film (91.3 Ω)(curve A), indicting superior conductivity of the π-conjugated D–π–A polymer. Subsequently, the R_{ct} increased gradually when Ab_1 (769.5 Ω) (curve C), BSA (1399.6 Ω) (curve D) and HIgG (1872.1 Ω) (curve E) were immobilized layer by layer on the resultant GCE. When labled Ab_2 was introduced to the sensor, the R_{ct} further increased (2911.9 Ω) (curve F), indicating that the immunosensor was established successfully.

3.5. Performance of the immunosensor for the detection of HIgG

To achieve an optimal analytical performance, related experimental conditions were performed in Supplementary material. Electrocatalytic current responses to H_2O_2 increased linearly with the rise of concentration of HIgG in the range of 0.1 pg mL^{-1} to 100 ng mL^{-1} (Fig. 5). The linear regression equation could be expressed as ΔI (μA) = 0.434 log c (pg mL^{-1}) + 1.2892 (R = 0.996). The limit of detection (LOD) was 0.06 pg mL^{-1}, using equation of LOD = 3σ/S where σ is the standard deviation of the blank response and S is the slope of calibration curve. Table S1 compared the present work's figures of merit to the recent reported values in the literature.

3.6. Selectivity, reproducibility and stability of the immunosensor

Specificity is an important criterion for electrochemical

Table 1
Recovery of HIgG from serum samples.

Sample	Added ($ng\,mL^{-1}$)	Found[a] ($ng\,mL^{-1}$)	RSD (%)	Recovery (%)
1	0.01	0.0107	3.25	107.0
2	0.10	0.106	3.26	106.0
3	1.00	1.03	3.02	103.0
4	30.00	31.3	2.99	104.3
5	100.00	102.5	2.96	102.5

[a] Average of five determinations.

immunosensor. The ΔI of the prepared biosensor to $10\,ng\,mL^{-1}$ solutions of glucose oxidase, BSA, glucose, dopamine, L-proline, and L-cysteine were studied (Fig. S7). Much stronger current was observed for $1\,ng\,mL^{-1}$ HIgG than other potentially interfering substances, proving the special identification of target antigen. The currents upon introduction of interferents were virtually unchanged, in comparison with $1\,ng\,mL^{-1}$ HIgG alone, served as a proof-of-concept that the immunosensor exhibited a satisfactory specificity. The reproducibility of the biosensor was expressed in term of values for relative standard deviation (RSD) of five individual electrodes incubated with $1\,ng\,mL^{-1}$ HIgG (Fig. S8a). The RSD was less than 5%, demonstrating the repeatability of the substrate polymerization, reversibility of the antigen-antibody recognition and reliability of the labeled nanoparticle response. Therein, the stability of the immunosensor was assessed by measuring the fabricated sensing interfaces at 4 °C for a period (30 days). Over 93.6% of the initial value for $1\,ng\,mL^{-1}$ HIgG had retained, which was desirable compared to the stability of other developed sensors (Fig. S8b).

3.7. Determination of HIgG in real samples

To validate the prepared immunosensor capabilities for human serum analysis, different amounts of HIgG were added into 100× diluted serum samples for recovery tests. After five amperometric measurements for concentration of HIgG variation from 0.01 to $100\,ng\,mL^{-1}$ in real samples, the recoveries of the spiked samples varied from 102.5% to 107.0% (Table 1), with a RSD of less than 4.62%. Negative controls in serum samples also demonstrated little nonspecific binding in agreement with previous studies. These results indicate that this electrochemical immunoassay has a good accuracy for quantitative detection of HIgG even under biofouling effect introduced by serum addition.

4. Conclusions

In summary, the robust signal amplification of this biosensor is achieved through the application of highly active sites of the twinned Au-Pt core-shell boundaries as the signal tags and intriguing signal-generated characteristic of D–π–A conjugated polymers as the powerful electron transfer platform. As a result, the novel nonenzymatic sandwich-type immunosensor exhibits a wider linear range from $0.1\,pg\,mL^{-1}$ to $100\,ng\,mL^{-1}$ and a lower limit of detection ($0.06\,pg\,mL^{-1}$) with longer stability toward HIgG detection. Given the latest progresses in the field of nanobiotechnology and organic bioelectronics, this new method opens an avenue for combining together their properties and functionalities. Our investigations along this field are in progress.

Acknowledgements

This work acknowledges support from the National Natural Science Foundation of China (No. 21375045) and Natural Science Foundation of Jilin Province (No. 20180101195JC).

Appendix A. Supplementary material

Supplementary data associated with this article can be found in the online version at http://dx.doi.org/10.1016/j.bios.2018.03.016.

References

Ali, I., Lone, M.N., Aboulenein, H.Y., 2017. Medchemcomm.
Kumar, S. Ashok, Chen, S.L., Chen, S.M., 2009. Electroanalysis 21, 1379–1386.
Ashraf, R.S., Meager, I., Nikolka, M., Kirkus, M., Planells, M., Schroeder, B.C., Holliday, S., Hurhangee, M., Nielsen, C.B., Sirringhaus, H., McCulloch, I., 2015. J. Am. Chem. Soc. 137, 1314–1321.
Aydemir, N., Malmstrom, J., Travas-Sejdic, J., 2016. Phys. Chem. Chem. Phys. 18, 8264–8277.
Bian, T., Zhang, H., Jiang, Y., Jin, C., Wu, J., Yang, H., Yang, D., 2015. Nano Lett. 15, 7808–7815.
Chen, X., Wang, F., Chen, Z., 2008. Anal. Chim. Acta 623, 213.
Gao, Z., Xu, M., Hou, L., Chen, G., Tang, D., 2013. Anal. Chem. 85, 6945.
Gao, Z., Xu, M., Lu, M., Chen, G., Tang, D., 2015. Biosens. Bioelectron. 70, 194–201.
Gilroy, K.D., Ruditskiy, A., Peng, H.-C., Qin, D., Xia, Y., 2016. Chem. Rev. 116, 10414–10472.
Golubnitschaja, O., Flammer, J., 2007. Surv. Ophthalmol. 52 (Suppl 2) (S155).
Gu, Y., Yuan, R., Yan, X., Li, C., Liu, W., Chen, R., Tang, L., Zheng, B., Li, Y., Zhang, Z., 2015. Anal. Chim. Acta 889, 113.
Guo, X., Kulkarni, A., Doepke, A., Halsall, H.B., Iyer, S., Heineman, W.R., 2012. Anal. Chem. 84, 241–246.
Hackett, A.J., Malmström, J., Travas-Sejdic, J., 2017. Prog. Polym. Sci. 70, 18–33.
Jun, Y.W., Huh, Y.M., Choi, J.S., Lee, J.H., Song, H.T., Kim, S., Yoon, S., Kim, K.S., Shin, J.S., Suh, J.S., Cheon, J., 2005. J. Am. Chem. Soc. 127, 5732–5733.
Kang, C., Kang, J., Lee, N.S., Yoon, Y.H., Yang, H., 2017. Anal. Chem. 89, 7974–7980.
Kul, D., Pauliukaite, R., Brett, C.M.A., 2011. J. Electroanal. Chem. 662, 328–333.
Kulhánek, J., Bureš, F., 2012. Beilstein J. Org. Chem. 8, 25–49.
Kulhanek, J., Bures, F., 2012. Beilstein J. Org. Chem. 8, 25–49.
Lin, Y.X., Zhou, Q., Lin, Y.P., Tang, D.P., Niessner, R., Knopp, D., 2015. Anal. Chem. 87, 8531–8540.
Liu, H., Liu, C., Gu, Y., Li, C., Yan, X., Zhang, T., Lu, N., Zheng, B., Li, Y., Zhang, Z., Yang, M., 2018. Biosens. Bioelectron. 99, 296–302.
Long, R., Casanova, D., Fang, W.-H., Prezhdo, O.V., 2017. J. Am. Chem. Soc. 139, 2619–2629.
Melkonyan, F.S., Zhao, W., Drees, M., Eastham, N.D., Leonardi, M.J., Butler, M.R., Chen, Z., Yu, X., Chang, R.P.H., Ratner, M.A., Facchetti, A.F., Marks, T.J., 2016. J. Am. Chem. Soc. 138, 6944–6947.
Molina, P., Tárraga, A., Otón, F., 2012. Org. Biomol. Chem. 43, 1711–1724.
Pedone, D., Moglianetti, M., De Luca, E., Bardi, G., Pompa, P.P., 2017. Chem. Soc. Rev. 46, 4951–4975.
Qi, M., Zhang, Y., Cao, C.M., Zhang, M.X., Liu, S.H., Liu, G.Z., 2016. Anal. Chem. 88, 9614–9621.
Qin, W., Zhao, Y., Du, B., Dan, W., Cai, Y., Mao, K., He, L., Xu, C., 2011. Adv. Funct. Mater. 21, 4193–4198.
Ran, B., Xianyu, Y.L., Dong, M.L., Chen, Y.P., Qian, Z.Y., Jiang, X.Y., 2017. Anal. Chem. 89, 6114–6120.
Ranzoni, A., den Hamer, A., Karoli, T., Buechler, J., Cooper, M.A., 2015. Anal. Chem. 87, 6150–6157.
Saikachi, H., Matsuo, J., 1964. Yakugaku zasshi: J. Pharm. Soc. Jpn. 84, 416–420.
Sharma, G.V.M., Ramesh, A., Singh, A., Srikanth, G., Jayaram, V., Duscharla, D., Jun, J.H., Ummanni, R., Malhotra, S.V., 2014. Medchemcomm 5, 1751–1760.
Simon, D.T., Gabrielsson, E.O., Tybrandt, K., Berggren, M., 2016. Chem. Rev. 116, 13009.
Song, Y., Xia, X., Wu, X., Wang, P., Qin, L., 2014. Angew. Chem. 53, 12451.
Sun, J.W., Lee, J.-H., Moon, C.-K., Kim, K.-H., Shin, H., Kim, J.-J., 2014. Adv. Mater. 26, 5684–5688.
Swager, T.M., 1998. Cheminform 29 (no-no).
Tang, Z., Wang, L., Ma, Z., 2016. Biosens. Bioelectron. 92.
Tobjörk, D., Österbacka, R., 2011. Adv. Mater. 23, 1935–1961.
Travers, A., 2002. John Wiley & Sons, Inc.,
Walsh, M.J., Yoshida, K., Kuwabara, A., Pay, M.L., Gai, P.L., Boyes, E.D., 2017. Nano Lett. 12, 2027–2031.
Wang, D.F., Li, Y.Y., Lin, Z.Y., Qiu, B., Guo, L.H., 2015a. Anal. Chem. 87, 5966–5972.
Wang, X., Choi, S.I., Roling, L.T., Luo, M., Ma, C., Zhang, L., Chi, M., Liu, J., Xie, Z., Herron, J.A., 2015b. Nat. Commun. 6, 7594.
Wang, X.Y., Hu, Y.H., Wei, H., 2016. Inorg. Chem. Front. 3, 41–60.
Wen, W., Yan, X., Zhu, C., Du, D., Lin, Y., 2017. Anal. Chem. 89, 138–156.
Wu, J., Qi, L., You, H., Gross, A., Li, J., Yang, H., 2012. J. Am. Chem. Soc. 134, 11880.
Wu, L., Qu, X., 2015. Chem. Soc. Rev. 44, 2963.
Xie, J., Xu, C., Kohler, N., Hou, Y., Sun, S., 2007. Adv. Mater. 19, 3163–3166.
Yamauchi, Y., Tonegawa, A., Komatsu, M., Wang, H., Liang, W., Nemoto, Y., Suzuki, N., Kuroda, K., 2012. J. Am. Chem. Soc. 134, 5100–5109.
Yan, L.-Q., Chen, Y., Sun, X.-F., You, M.-J., Chen, X.-D., Gu, Q., Zhang, Y.-M., 2017. Chem. Pap. 71, 627–637.
Zhag, Y., Tan, C., Fei, R.H., Liu, X.X., Zhou, Y., Chen, J., Chen, H.C., Zhou, R., Hu, Y.G., 2014. Anal. Chem. 86, 1115–1122.